Biosensors and Bioelectronics 146 (2019) 111756

Contents lists available at ScienceDirect

Biosensors and Bioelectronics

journal homepage: http://www.elsevier.com/locate/bios

Ultrathin PtNi nanozyme based self-powered photoelectrochemical aptasensor for ultrasensitive chloramphenicol detection

Xu Zhu [a,b], Lei Gao [c], Lin Tang [a,b,*], Bo Peng [a,b], Hongwen Huang [c,**], Jiajia Wang [a,b], Jiangfang Yu [a,b], Xilian Ouyang [a,b], Jisui Tan [a,b]

[a] College of Environmental Science and Engineering, Hunan University, Changsha, 410082, China
[b] Key Laboratory of Environmental Biology and Pollution Control (Hunan University), Ministry of Education, Changsha, 410082, Hunan, China
[c] College of Materials Science and Engineering, Hunan University, Changsha, Hunan, 410082, PR China

ARTICLE INFO

Keywords:
Ultrathin PtNi nanozyme
Self-powered
Photoelectrochemical aptasensor
Benzene-ring doped
g-C_3N_4
Chloramphenicol

ABSTRACT

Nanozymes have gained increasing attention in the field of biosensing. Rationally designed nanozymes with excellent catalytic activity are accessible to substitute natural enzymes. Herein, a novel self-powered photoelectrochemical (PEC) aptasensor was constructed for ultrasensitive detection of chloramphenicol (CAP) based on ultrathin PtNi nanowires (NWs) as nanozyme and benzene-ring doped g-C_3N_4 (BR-CN) as the photoactive material. The prepared 1-nm-thick PtNi nanozyme acted as a peroxidase, possessing higher catalytic activity than natural horseradish peroxidase (HRP) and other Pt-based mimic enzymes. Through the biotin-streptavidin specific interaction, streptavidin modified PtNi nanozyme was introduced into the dual-stranded DNA (dsDNA) formed by complementary DNA and biotinylated CAP aptamer. The PtNi nanozyme catalyzed 4-chloro-1-naphthol (4-CN) oxidation to generate insoluble precipitation on the electrode surface, resulting in an obvious photocurrent reduction. In the presence of CAP, the CAP aptamer was released from the electrode due to strong affinity with CAP, causing the decrease of catalytic precipitation and consequently the generation of a high photocurrent signal. On the basis of PtNi nanozyme signal amplification, the developed self-powered PEC aptasensor showed a wide linear range of 0.1 pM–100 nM with an ultralow detection limit of 26 fM for the determination of CAP. This work provides a feasible strategy for the design of high-activity nanozyme and self-powered PEC biosensor to achieve the ultrasensitive detection of target analyte.

1. Introduction

Photoelectrochemical (PEC) aptasensor, as a promising analytical technique for trace detection, has attracted extensive attention due to its high selectivity and sensitivity, rapid response and easy miniaturization (Tang et al., 2019; Zang et al., 2017). Moreover, self-powered PEC aptasensor can work without extra voltage, efficiently eliminating possible interference from other substances (Peng et al., 2018; Shang et al., 2019). Signal amplification is essential for PEC aptasensor to obtain high sensitivity. Various methods have been applied, such as enzymatic reactions (Wang et al., 2018a), steric hindrance effects (Fan et al., 2016), and quenching effects (Huang et al., 2019a). Thereinto, the enzyme-mediated catalytic precipitation (CP) is a simple and effective strategy, which can generate insoluble products on the electrode surface and further cause the change of photocurrent signal (Wang et al., 2019; Zhao et al., 2011). However, the natural enzymes, such as horseradish peroxidase (HRP) and alkaline phosphate (ALP), generally suffer from poor stability, high cost, and harsh conditions for storage. To overcome these shortcomings, nanozymes, a class of nanomaterials with enzyme-like characteristics, have emerged as a promising alternative because of the good stability and low cost. Nowadays, a large variety of inorganic nanomaterials, including transition metal oxides (Gao et al., 2007), noble metals (Oh et al., 2018) and carbon nanomaterials (Song et al., 2010) have been developed to design mimetic enzymes. And several peroxidase-like nanomaterials have been exploited to the PEC biosensors. For instance, the histidine-modified Fe_3O_4 nanozyme could serve as peroxidase to generate the insoluble precipitation in a PEC immunoassay (Li et al., 2019). A PEC assay using the Co_3O_4–Au polyhedra as peroxidase mimic to produce CP was developed (Yang et al., 2018). Thus, a novel and high-activity peroxidase-mimic nanozyme may

* Corresponding author. College of Environmental Science and Engineering, Hunan University, Changsha, 410082, China.
** Corresponding author.
E-mail addresses: tanglin@hnu.edu.cn (L. Tang), huanghw@hnu.edu.cn (H. Huang).

https://doi.org/10.1016/j.bios.2019.111756
Received 19 July 2019; Received in revised form 30 September 2019; Accepted 1 October 2019
Available online 3 October 2019

provide a new method for the design of PEC aptasensing strategy.

The Pt-based nanomaterials are well-approved with strong peroxidase-mimic catalytic activities and have been widely used to construct a sensing platform (Mu et al., 2019; Wang et al., 2015). However, the noble metal Pt is rare on the earth and high cost, which extremely restricts its application potential. Therefore, it is crucial to rationally design the composition and structure of Pt-based nanomaterials for the improvement of catalytic performance and utilization efficiency (Fu et al., 2019). Incorporating the non-noble metals (such as Cu, Fe, Ni) into Pt-based alloys is an effective strategy to improve the catalytic ability because of synergistic effect between the different components (Hu et al., 2019; Wang et al., 2018b). Furthermore, the intrinsic catalytic properties of Pt-based alloys are closely related to their shape, size, and morphology (Lu et al., 2016b). Recently, one-dimensional (1D) Pt-based ultrathin nanowires (NWs) have attracted vast interest owing to the structurally induced physicochemical properties. Compared with other structures, 1D ultrathin NWs have many merits including anisotropy, high surface area, and increasingly exposed crystal planes, which can improve the stability and catalytic activity (Song et al., 2018). Inspired by the above research, the ultrathin PtNi NWs with 1-nm-thick diameter were synthesized, which showed high peroxidase-like activity and affinity to the substrates. To date, the design and application of ultrathin PtNi NWs as nanozyme for PEC aptasensing have not been reported.

To support the CP-based signal amplification, proper photoactive materials with high-efficiency photoelectric conversion are also necessary. Graphitic carbon nitride (g-C_3N_4) has attracted widespread concerns in PEC biosensing because it possesses unique electronic and optical properties (Hua et al., 2018; Tang et al., 2019). However, pure g-C_3N_4 shows unsatisfactory performance owing to the rapid recombination speed of photogenerated electron-hole pairs, insufficient visible-light absorption and low specific surface areas, which extremely hampers its practical applications (Deng et al., 2018; Tang et al., 2018a). In order to address these drawbacks, numerous approaches have been adopted, including regulating morphology structure (Han et al., 2016), constructing heterostructures (Wang et al., 2017), heteroatom doping (Wu et al., 2018), and so on. In particular, introducing benzene-ring structure into the network of g-C_3N_4 is an effective method, due to the extended delocalization of π-electrons and regulated electronic band structure (Li et al., 2018b; Zhou et al., 2018). For instance, Yu et al. recently synthesized a kind of benzene-ring doped g-C_3N_4 (BR-CN) through copolymerizing m-trihydroxybenzene with urea, which remarkably improved the harvesting visible-light ability, achieving unimpeded separation and transfer of photo-induced carriers (Yu et al., 2017). Thus, BR-CN as the photoactive material applied to the PEC sensing platform will be a good choice.

Chloramphenicol (CAP) as a broad-spectrum antibiotic was universally used in the disease prevention and treatment for human and animal husbandry due to its low cost and high efficiency in antibacterial effect (Pilehvar et al., 2012). However, CAP residues have been found in the rivers and even animal-derived food products such as honey, eggs and milk because of illegal use of CAP (Guo et al., 2017; Yu et al., 2019), which seriously threatens human health. Currently, various analytical techniques have been employed for CAP determination, such as high performance liquid chromatography (Lu et al., 2016a), liquid chromatography-mass spectrometry (Kikuchi et al., 2017) and gas chromatography-mass spectrometry (Chang et al., 2016). However, these methods involve sophisticated equipment, complicated operation procedures and time-consuming sample preparation. Additionally, a series of simple and effective colorimetric and electrochemical sensors have been developed (El-Moghazy et al., 2018; Yan et al., 2018), but their sensitivities need to be further improved. Therefore, it is essential to develop a simple, rapid, highly selective and sensitive analytical method for quantitative determination of CAP.

In this work, we rationally applied the ultrathin PtNi nanozyme into the BR-CN constructed PEC sensing platform for CAP detection. The PtNi nanozyme was derived from ultrathin PtNi NWs, exhibiting high peroxidase-like activity. And the BR-CN was prepared by a facile thermal copolymerization of urea with 4,4′-sulfonyldiphenol (BPS) and showed excellent PEC performance, achieving self-powered demand. In addition, we designed a novel signal amplification strategy, which coupled the PtNi nanozyme stimulated CP with target CAP induced photocurrent change. This developed self-powered PEC aptasensor exhibited good selectivity, repeatability, stability, and satisfactory practical sample analysis ability.

2. Experimental

2.1. Materials and apparatus

The relevant materials, reagents, and apparatus used in this work are described in the “Supporting Information”.

2.2. Synthesis of ultrathin PtNi NWs

The ultrathin PtNi NWs were synthesized by previous method with minor modification (Li et al., 2018a). $Pt(acac)_2$ (20 mg), $Ni(acac)_2$ (10 mg), cetyltrimethylammonium bromide (CTAB, 75 mg) and 4 mL oleylamine were added into a 30 mL vial. Then, the resulting mixture was preheated in an oil bath and kept at 170 °C for 5 min. Subsequently, 10 mg of $W(CO)_6$ was rapidly added into the above solution to initiate the reaction, and the reaction was allow to proceed for 2 h. The product was collected by centrifugation and subsequently washed three times with ethanol and hexane (1:2, v/v). Next, it was transferred into the mixture solution containing 4 mL ethanol and 1 mL diethylamine for 24 h, and then centrifuged. The final product was dispersed in ethanol for further use. The synthesis of Pt NWs was similar procedure except for the absence of Ni precursors.

The synthesis of streptavidin modified ultrathin PtNi NWs (SA-PtNi) was described as below. 100 μL of SA (1 mg mL^{-1}) was added into 1 mL of PtNi NWs aqueous suspension (0.5 mg mL^{-1}), and the mixed solution was shook gently for 12 h at 4 °C to make SA immobilize onto the PtNi NWs via the Pt–NH_2 bond (Cui et al., 2018; Xu et al., 2018). The SA-PtNi was obtained by centrifugation and then washed with ultrapure water to remove the unbound SA. Finally, the SA-PtNi was redispersed in 500 μL Tris-Hcl buffer and stored at 4 °C for further experiment.

2.3. Peroxidase-like activity and kinetic analysis of the ultrathin PtNi NWs

To verify the peroxidase-like activity of ultrathin PtNi NWs, the 3,3′,5,5′-tetramethylbenzidine (TMB) was used as chromogenic substrate for study. Specifically, 5 μg mL^{-1} of ultrathin PtNi NWs were added into 3 mL sodium acetate buffer (pH 4.0) containing 25 mM H_2O_2 and 100 μM TMB. After reaction for 3 min, the resulting mixed solution was carried out UV–vis scanning by a UV–vis spectrophotometer. The peroxidase-like activity was assessed by monitoring the absorbance value at 652 nm (Sui et al., 2019).

The steady-state kinetic assays were performed in time-course mode, and all of measurements were monitored by the absorbance change at 652 nm. The experiments were carried out in 3 mL sodium acetate buffer (pH 4.0) with diverse concentrations of TMB and H_2O_2. The kinetic parameters were calculated according to the typical Michaelis-Menten equation: $\nu = V_{max} \times [S]/(K_m + [S])$, where ν represents the initial velocity, V_{max} represents the maximal reaction velocity, K_m represents the Michaelis constant, and [S] represents the substrates concentration (Kim et al., 2019).

2.4. Synthesis of BR-CN nanosheets

The BR-CN nanosheets were synthesized by a thermal copolymerization method (Liu et al., 2019). Typically, 20 g of urea and 20 mg of

BPS were mixed uniformity, and then the obtained mixture was placed into a ceramic crucible with a cover. Subsequently, the crucible was heated to 550 °C with a rising rate of 2.3 °C min^{-1} and maintained for 4 h in a muffle furnace. The resulted powder was transferred into a rectangle crucible for heat etching process without cover, with a rising rate of 10 °C min^{-1} to 500 °C and kept for 2 h. The ultimately obtained brown powder was denoted as BR-CN. In comparison, pure g-C_3N_4 nanosheets were synthesized in a similar procedure without the addition of BPS.

2.5. Construction of the PEC aptasensor

The construction process of the PEC aptasensor is shown in Scheme 1A. Prior to the modification, the bare fluorine-doped tin oxide (FTO) electrodes (1.0 cm × 2.0 cm) were thoroughly rinsed with acetone, ethanol and ultrapure water in the successive sonication, respectively, and dried with nitrogen gas. First, 200 μL of BR-CN suspension (4 mg mL^{-1}, dispersed into mixed solution of ethanol and 0.05% Nafion) was coated onto FTO electrode and dried, the BR-CN/FTO electrode was obtained. 20 μL of 0.1 wt% chitosan (CS) (dissolved in 1% acetic acid) was decorated on the FTO electrode and dried at 50 °C. Then, 20 μL of 5 wt% glutaraldehyde (GLD) was further dripped on the modified electrode and kept for 30 min at the room temperature. GLD was used as cross linker to combine both CS and amine-functionalized complementary DNA (cDNA) via forming two amide bonds. Subsequently, the electrode was washed several times with ultrapure water to remove unbound GLD. After each subsequent modification process, the electrode was cleaned with washing buffer. Specifically, 20 μL of immobilization buffer containing 1 μM cDNA was dropped onto the electrode and incubated for 12 h at 4 °C. In order to block the non-specific binding sites, 10 μL of 1 wt% BSA was cultured on modified electrode for 1 h at room temperature. Then, 20 μL of hybridization solution containing 1 μM CAP aptamer was further added to electrode surface to conduct DNA hybridization reaction for another 1 h at 37 °C. Eventually, the aptasensor was obtained and stored in refrigerator at 4 °C after drying in nitrogen for further usage.

2.6. Measurement procedure

20 μL of CAP solution with different concentrations was added onto the constructed aptasensor and incubated at 37 °C for 40 min. After washing carefully, 20 μL of SA-PtNi suspension was coated on the electrode and incubated at 37 °C for 2 h. The SA-PtNi was introduced to aptasensor by the specific binding between SA and biotin. Finally, the modified electrode was incubated in the 1 mM 4-chloro-1-naphthol (4-CN) solution containing 0.15 mM H_2O_2 at room temperature for 20 min. The PEC measurement was performed in Tris-HCl buffer (pH 7.4, 0.1 M), and the bias voltage was 0 V.

3. Results and discussion

3.1. Detection principle of the PEC aptasensor

The principle of the constructed PEC aptasensor for CAP determination is illustrated in Scheme 1B. After the stepwise modified processes, the biotinylated CAP aptamer (Bio-Aptamer) was anchored onto the BR-CN/FTO through hybridization reaction with cDNA and formed dual stranded DNA (dsDNA). In the absence of CAP, PtNi nanozyme was introduced the sensor via the biotin-streptavidin specific interaction. Because of the excellent peroxidase-like activity, the PtNi nanozyme

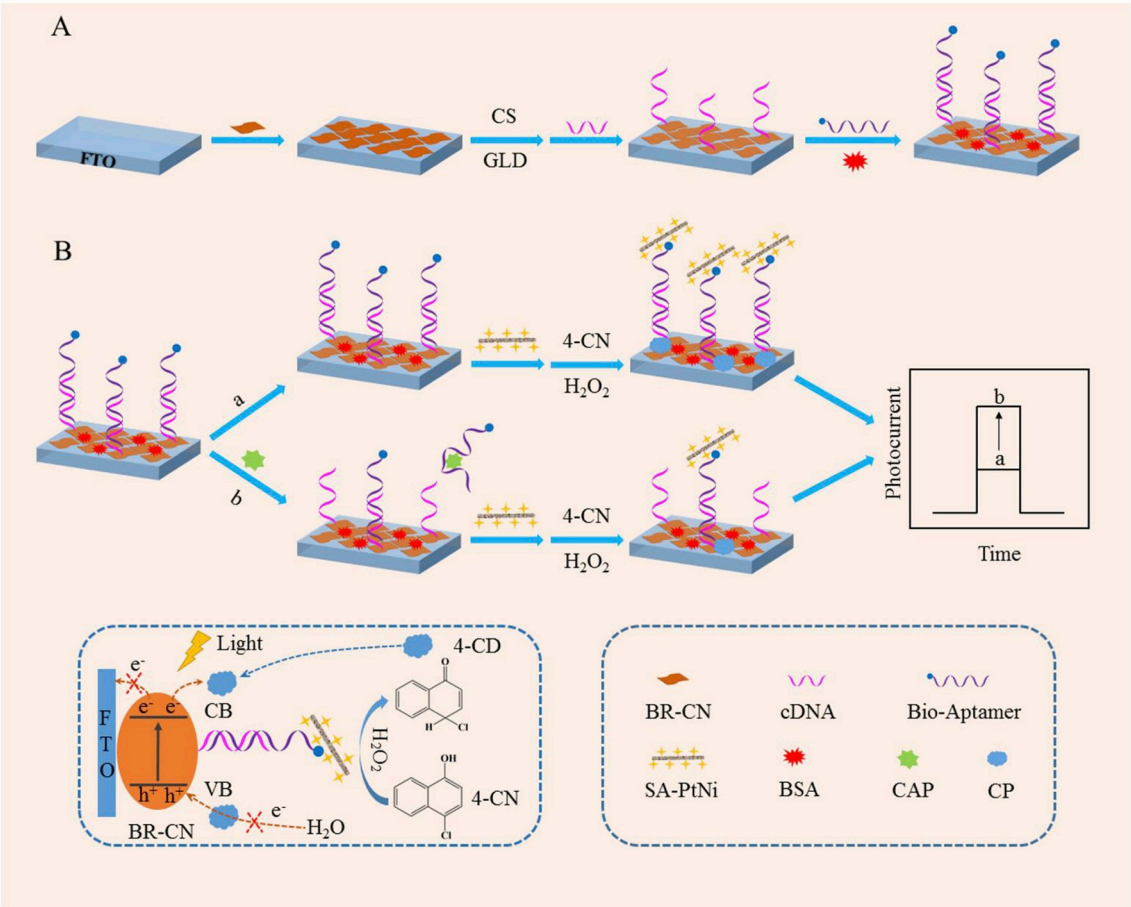

Scheme 1. (A) Schematic illustration of the aptasensor construction process, and (B) the mechanism of PEC aptasensor for CAP determination.

catalyzed 4-CN oxidation by H_2O_2 to produce insoluble benzo-4-chlorohexadienone (4-CD) on the electrode surface. In order to generate the photocurrent signal on BR-CN/FTO, H_2O as electron donor could provide the electron to hole of BR-CN, and the photoexcited electron that accumulated on the CB of BR-CN could transfer to FTO (Chen et al., 2017; Liu et al., 2019). However, the insoluble 4-CD could hinder the reaction between H_2O and BR-CN, which cut down the hole trapping ability of H_2O for BR-CN. In addition, the oxidized 4-CD as electron acceptor could also accept the photoexcited electrons from CB of BR-CN, reducing the electrons that transferred to FTO. Thus, the photocurrent was remarkably decreased (Gong et al., 2016; Wang et al., 2019). When incubated with CAP, the dsDNA structure was dissociated and the CAP aptamer was released from the electrode surface due to strong affinity between aptamer and CAP (Chen et al., 2018; Huang et al., 2019b; Yan et al., 2018). Thus, a lower amount of PtNi nanozyme was captured, leading to the decrease of CP and consequently the enhancement of photocurrent signal. According to the dose-responsive relation between the CAP concentration and the PEC signal, ultrasensitive detection of CAP could be achieved.

3.2. Characterizations of the ultrathin PtNi NWs

The morphology and microstructure of ultrathin PtNi NWs were characterized by the transmission electron microscopy (TEM) and high-angle annular dark-field scanning transmission electron microscopy (HAADF-STEM). As shown in Fig. 1A–B, the products present well-dispersed 1D NWs morphology with high purity. The average diameter of NWs was measured to be about 1.2 nm, indicating that the synthesized NWs possessed ultrathin structure. The atomic-resolution HAADF-STEM image of an individual PtNi NW exhibits that the NW is five or six atomic layers thick, consistent with the average diameter. In addition, the single-crystalline property of the NWs was confirmed by the continuous lattice fringes (Fig. 1C). The energy-dispersive X-ray spectroscopy (EDX) was employed to investigate the elemental composition. As shown in Fig. 1D, the elemental mapping images of the prepared samples demonstrate that Pt and Ni were homogeneous throughout the whole structure. The X-ray diffraction (XRD) patterns (Fig. 1E) of the PtNi NWs show a typical fcc structure and all characteristic diffraction peaks have slight blue shift relative to the Pt NWs due to the coupling of partial Ni atoms (Zhang et al., 2019), further illustrating that the alloy structure was synthesized successfully. Moreover, as determined by the inductively coupled plasma atomic emission spectroscopy (ICP-AES), the atomic ratio of Pt and Ni was proved to be about 2.99:1.00.

3.3. Peroxidase-like activity of the PtNi nanozyme

To investigate the catalytic performance of the synthesized ultrathin PtNi nanozyme, the peroxidase-like mediated oxidation reactions were performed by using the typical chromogenic substrate TMB in the presence of H_2O_2. As exhibited in Fig. 2A, no obvious absorption peaks are observed without the addition of PtNi NWs into the systems containing TMB, regardless of whether H_2O_2 existed or not (curve a and b). However, after the addition of PtNi NWs into the system with the coexistence of H_2O_2 and TMB, a strong absorption peak at 652 nm appears instantly (curve d), demonstrating that the synthesized ultrathin PtNi NWs owned prominent peroxidase-like ability. Apparently, PtNi NWs showed a higher absorption value than Pt NWs (curve c), indicating a higher catalytic activity. It was ascribed to the synergistic effect of Pt and Ni (Jiang et al., 2019). Moreover, compared with the HRP, the catalytic activities of both PtNi NWs and Pt NWs were higher (curve e). It was because that the ultrathin NWs structure improved the catalytic activity on account of more exposed surface areas, which could remarkably increase the utilization efficiency of Pt atoms (Huang et al., 2017).

In order to further understand the catalytic mechanism, the steady-state kinetic assays were performed. As shown in Fig. 2B, the typical Michaelis-Menten curve toward TMB was obtained by fixing H_2O_2 concentration while varying TMB concentration with a certain range. According to Lineweaver-Burk double reciprocal plot, the corresponding kinetic parameters were calculated (inset in Fig. 2B). Similarly, the steady-state kinetic of H_2O_2 also exhibited typical Michaelis-Menten

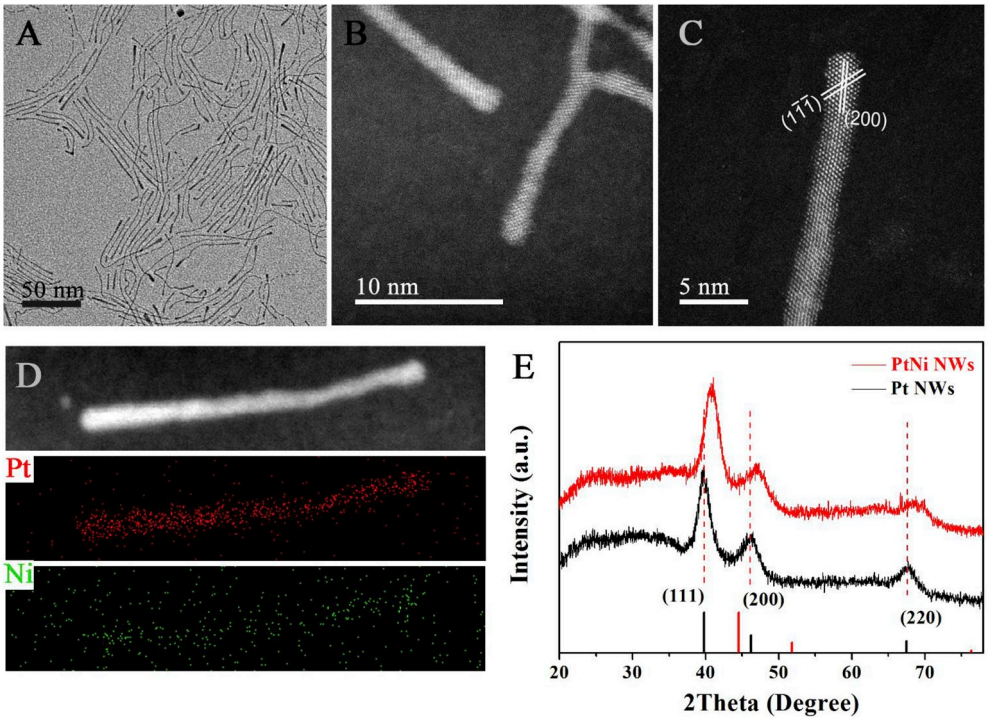

Fig. 1. (A) TEM image, (B) HAADF-STEM image, and (C) Atomic-resolution HAADF-STEM image of PtNi NWs; (D) EDX elemental mapping images of Pt and Ni; (E) XRD patterns of PtNi NWs and Pt NWs.

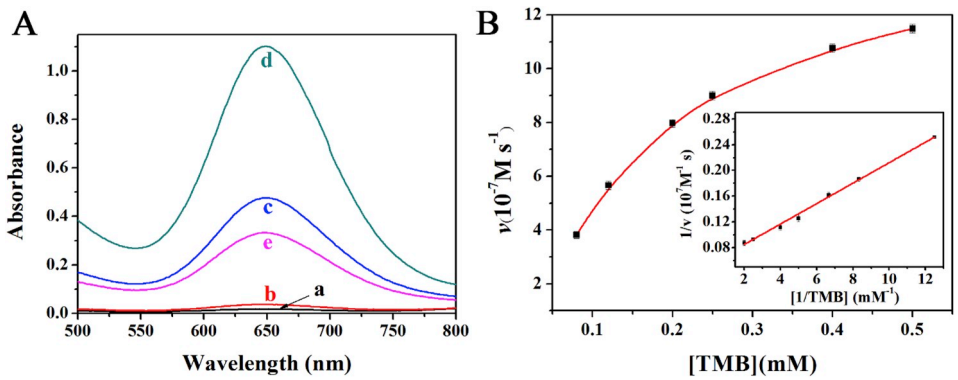

Fig. 2. (A) UV–vis absorption spectra in different reaction systems: (a) TMB, (b) TMB-H_2O_2, (c) Pt NWs-TMB-H_2O_2, (d) PtNi NWs-TMB-H_2O_2 and (e) HRP-TMB-H_2O_2 in the sodium acetate buffer (pH 4.0) after 3 min of reaction; (B) The steady-state kinetic assay of TMB oxidation by PtNi NWs with fixed H_2O_2 concentration (inset: the corresponding Lineweaver-Burk double reciprocal plot).

curve (Fig. S1). And the results are listed in Table S2. The K_m mirrors the affinity between substrates and enzyme with a lower K_m value meaning a higher affinity (Karim et al., 2018). The K_m values of PtNi nanozyme were determined to be 0.31 mM for TMB and 1.2 mM for H_2O_2, which were both lower than that of natural HRP, indicating that PtNi nanozyme possessed a higher affinity for both TMB and H_2O_2. Meanwhile, the V_{max} of PtNi nanozyme with TMB and H_2O_2 as the substrates were much higher than HRP and other Pt-based nanomaterials, originating from the unique structure of PtNi NWs and the synergistic effect, further suggesting high peroxidase-like activity of synthesized PtNi nanozyme.

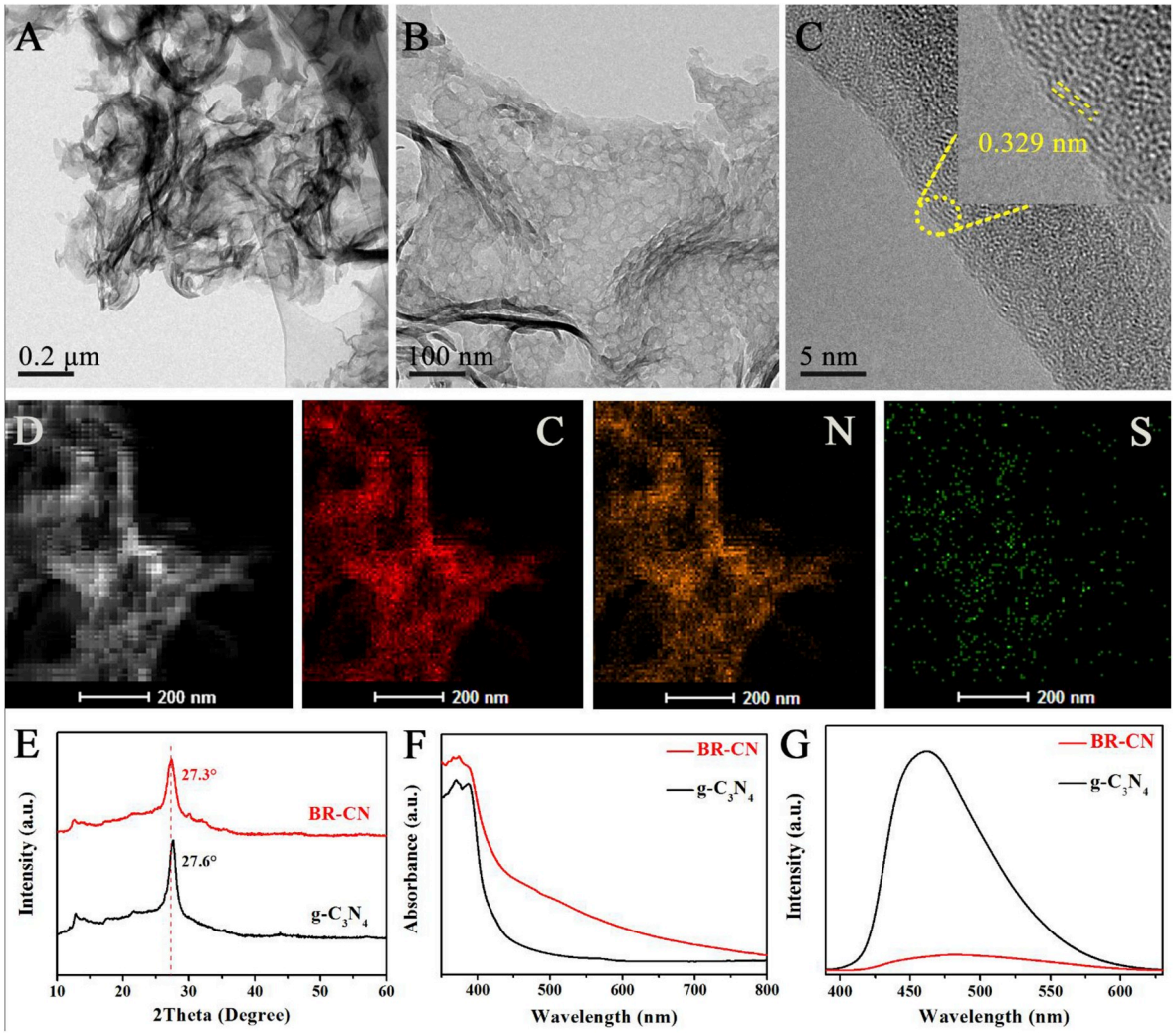

Fig. 3. (A–B) TEM and (C) HRTEM images of BR-CN; (D) HAADF-STEM image and EDS elemental mapping of BR-CN; (E) XRD patterns, (F) UV–vis diffuse reflectance spectra, and (G) PL spectra.

3.4. Characterization of the BR-CN nanosheets

The synthetic pathway of BR-CN is illustrated in Scheme S1. BPS participated in the polymerization during the melamine formation step and was doped onto the g-C_3N_4 backbone through copolymerization. The morphology feature of BR-CN nanosheets was characterized by TEM. As shown in Fig. 3A, BR-CN exhibits a sheet-like structure with many wrinkles (Fig. S2A), which is similar to pure g-C_3N_4 nanosheets (Feng et al., 2018). Meanwhile, a porous structure of BR-CN can be clearly observed (Fig. 3B). Further porosity analysis was conducted by N_2 adsorption-desorption experiments, where the typical type IV isotherms in Fig. S2C indicate the existence of mesopores (Tang et al., 2018b; Yu et al., 2017). The higher specific surface area of BR-CN (169.7 $m^2 g^{-1}$) than that of pure g-C_3N_4 (121.9 $m^2 g^{-1}$), while their pore diameter show no apparent change (inset in Fig. S2C). The increased specific surface area could expose more active sites, which was important for the PEC performance. The interlamellar spacing of BR-CN with 0.329 nm can be observed from the high-resolution TEM (HRTEM) image (Fig. 3C), which was a bit larger than pure g-C_3N_4 (~0.325 nm). The XRD patterns (Fig. 3E) show that one characteristic diffraction peak of BR-CN shifts to a lower angle from 27.6° in g-C_3N_4 to 27.3°, indicating the increase of stacking distance (Yu et al., 2018), which is consistent with the result of HRTEM. And the increased stacking distance might be ascribe to the introduced coplanar rings. Additionally, as proved by Fig. 3D, the C, N and S elements are uniformly distributed in the entire structure, suggesting that BPS were evenly incorporated into the g-C_3N_4 without self-polymerization. Besides, X-ray photoelectron spectroscopy (XPS) was employed to further characterize the chemical compositions of BR-CN and the detailed information is presented in the "Supporting Information" (Fig. S3).

The optical properties of BR-CN were analyzed by UV–vis diffuse reflectance spectra. As can be seen in Fig. 3F, the pure g-C_3N_4 nanosheets display the adsorption edge around 440 nm, while the BR-CN evidently extends the absorption range up to 800 nm. It can be reflected by the significant color difference between BR-CN and g-C_3N_4 (Fig. S2B). Hence, it was proved that introduction of benzene ring could improve light harvesting, which was conducive to enhance the PEC performance (Ge et al., 2019). The photoluminescence (PL) technology was also carried out (Fig. 3G). On account of the fast recombination of photo-induced electrons and holes, pure g-C_3N_4 displays a strong emission peak near 460 nm, while a precipitously descending intensity can be observed in BR-CN. Meanwhile, the peak of BR-CN shifts to the longer wavelength. This phenomenon elucidated that the incorporation of benzene ring greatly facilitated the photogenerated charges separation. Based on the above analysis, it could be confirmed that the benzene ring was successfully introduced into the skeleton of g-C_3N_4 nanosheets via the thermal co-polymerization strategy.

The PEC behavior was performed under visible-light irradiation. As shown in Fig. 4A, the g-C_3N_4/FTO exhibits a weak photocurrent response owing to insufficient absorption of visible light. Nevertheless, the photocurrent intensity of BR-CN/FTO significantly enhances, which is about 5-fold higher than that of g-C_3N_4/FTO. This phenomenon was ascribed to wide absorption range in visible-light region and effective separation of photogenerated charges. Additionally, the electrochemical impedance spectroscopy (EIS) measurement was employed to further investigate the interface charge transfer process (Feng et al., 2019). The equivalent circuit (inset in Fig. 4B) includes solution resistance (R_s), charge transfer resistance (R_{ct}), warburg impedance (Z_w) and interfacial capacitance (C_{dl}). Generally, the semicircle diameter of Nyquist plot represents R_{ct} value (Tang at al. 2009). As presented in Fig. 4B, the R_{ct} value BR-CN/FTO is much lower than that of g-C_3N_4/FTO, indicating that the introduction of benzene ring could promote the charge transfer.

3.5. Characterization of the developed PEC aptasensor

The photocurrent responses were used to investigate the stepwise construction process. As displayed in Fig. 5A, the BR-CN/FTO electrode showed a remarkable photocurrent intensity (curve a). After the successive introduction of CS, cDNA and BSA on the BR-CN/FTO electrode, the photocurrents gradually decreased (curves b-d). That was because the poor conductivity of CS and increased steric hindrance effects of cDNA and protein molecules hindered the electron diffusion between BR-CN and H_2O, leading to the decrease of photocurrent (Cheng et al., 2018; You et al., 2019). After interaction with the CAP aptamer, the photocurrent further decreased (curve e). It could be attributed to the hybridization reaction between CAP aptamer and cDNA, leading to the formation of dsDNA. However, the photocurrent increased clearly (curve f) after incubating 100 pM of CAP followed by subsequent washing. This was because CAP had stronger affinity with its aptamer than that of the correlative dsDNA, causing the dissociation of partial dsDNA and release of the aptamer from the electrode surface (Liu et al., 2016). In addition, the photocurrent decreased after introducing of PtNi nanozyme due to the increase of steric hindrance caused by nonconductive SA (curve g). Notably, the photocurrent remarkably decreased after being incubated in the system with 4-CN and H_2O_2 coexisting (curve h), suggesting that PtNi nanozyme catalyzed the oxidization of 4-CN to form the insoluble 4-CD precipitates on the electrode surface, further hindering the hole trapping ability of H_2O for BR-CN. Meanwhile, the oxidized 4-CD could also accept the photogenerated electrons, which reduced the amount of electrons transferring to the FTO electrode. Thus, the above results demonstrated the successful construction of the developed PEC aptasensor.

EIS is also an effective technique to investigate the stepwise modified processes of the electrode. As shown in Fig. 5B, BR-CN/FTO electrode presented a relatively small R_{ct} (curve a). After the orderly assembly of weakly conductive CS, negatively charged cDNA and nonconductive BSA on the electrode, the R_{ct} values gradually increased (curves b-d). When incubated with the CAP aptamer, the R_{ct} value further increased (curve e), indicating the formation of dsDNA structure through the hybridization reaction, which further enhanced the effect of electrostatic

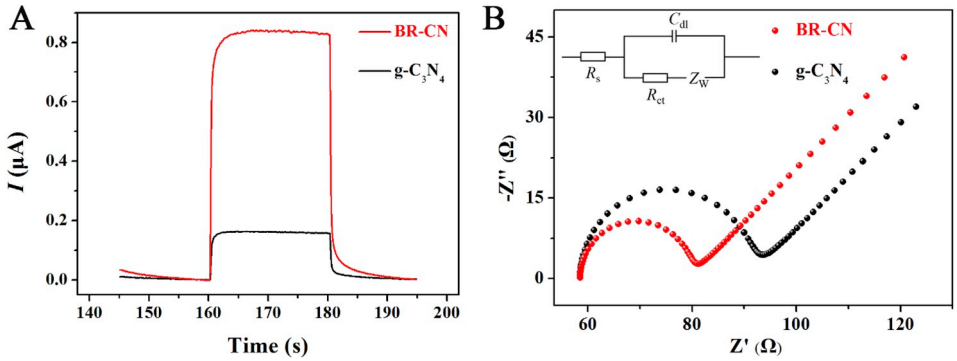

Fig. 4. (A) Photocurrent responses to light of wavelength above 420 nm, and (B) EIS spectra of BR-CN and g-C_3N_4.

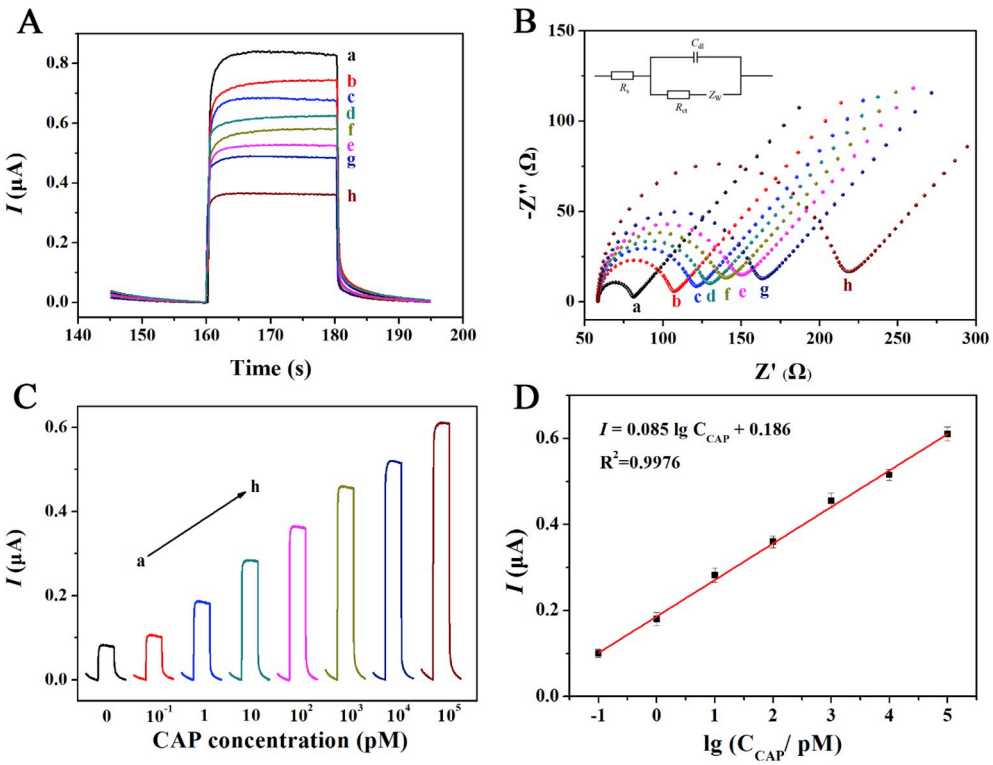

Fig. 5. (A) Photocurrent responses; (B) EIS spectra of (a) BR-CN/FTO, (b) after CS coating, (c) after cDNA immobilization, (d) after BSA blocking, (e) after hybridization with CAP aptamer, (f) after incubation with 100 pM CAP, (g) after further incubation with PtNi nanozyme, and (h) after finally incubation with H_2O_2 and 4-CN; (C) Photocurrent signal of modified electrode in the different CAP concentrations (from a to h: 0–100 nM); (D) Calibration curve for CAP on the PEC aptasensor. The error bars are derived from the standard deviations of three measurements.

repulsion with the negatively charged $[Fe(CN)_6]^{3-/4-}$. However, the R_{ct} value obviously decreased (curve f) after adding 100 pM of CAP with subsequent washing. It might be ascribed to the dissociation of partial dsDNA structure and release of the CAP aptamer from the electrode surface by washing thoroughly. After incubated with PtNi nanozyme, the R_{ct} value increased owning to the steric hindrance effect of the SA-PtNi (curve g). Finally, the R_{ct} value significantly enhanced after being incubated in the solution containing H_2O_2 and 4-CN (curve h), suggesting that the generation of insoluble precipitation catalyzed by the PtNi nanozyme. The detailed EIS results are shown in the "Supporting Information" (Table S3) and further demonstrated that the aptasensor was constructed successfully.

The catalytic activities of PtNi nanozyme, Pt nanozyme and HRP on the PEC aptasensor were also compared. As shown in Fig. S4A, the photocurrent change caused by incubation with PtNi nanozyme is much larger than those of Pt nanozyme and HRP, indicating the higher catalytic activity of PtNi nanozyme for the substrates of H_2O_2 and 4-CN, which generated more insoluble 4-CD precipitation on the electrode surface. This deduction was also confirmed by the EIS results (Fig. S4B). Thus, the PtNi nanozyme is optimal for signal amplification.

3.6. Optimization of experimental conditions

To achieve high analytical performance of the developed PEC aptasensor for CAP detection, several predominant experiment parameters were optimized, including the mass of added BPS, the incubation time and temperature of CAP and the catalytic precipitation time.

As shown in Fig. S5A, the maximum photocurrent intensity of BR-CN/FTO electrode was obtained when the mass of BPS was 20 mg, illustrating that the introduction of BPS with benzene structure could effectively improve the photogenerated charges separation. However, the photocurrent response decreased when the amount was more than 20 mg, which might ascribe to the destroyed basic structure of g-C_3N_4 by the excessive doping. Thus, 20 mg of BPS was chosen as the optimized mass.

The incubation time of CAP plays a key factor on the PEC response of the constructed aptasensor, because it directly affects the degree of dissociation of dsDNA. As exhibited in Fig. S5B, the photocurrent response enhanced gradually with the increasing incubation time of CAP up to 40 min, and then leveled off. Similarly, the intensity of photocurrent gradually increased with the incubation temperature increased and did not change much after 37 °C (Fig. S5C), indicating that the specific binding between aptamer and CAP reached to the saturation state. Therefore, 40 min and 37 °C were employed as the optimized time and temperature for CAP incubation in this study, respectively.

Fig. S5D displays the effect of the catalytic precipitation time on photocurrent signal. The photocurrent decreased with the increasing catalytic precipitation time because the longer catalytic time generated more insoluble 4-CD precipitates on the electrode surface and formed the greater steric hindrance, suppressing the electron transfer. Notably, the photocurrent value achieved a plateau after 20 min. Consequently, 20 min was taken as the optimized catalytic precipitation time.

3.7. PEC detection of CAP

Under the above optimized conditions, the PEC detection of CAP at various concentrations was investigated. As shown in Fig. 5C, the photocurrent of blank sample (0 pM) was measured to be 83.2 nA, and the photocurrent signals were enhanced with the increasing CAP concentration. Meanwhile, the photocurrent intensity was linear with the logarithm of CAP concentration in a wide range from 0.1 pM to 100 nM, and the corresponding linear regression equation was I (μA) = 0.085 lg C_{CPA} (pM) + 0.186 (R^2 = 0.9976) (Fig. 5D). The limit of detection (LOD, S/N = 3) was estimated to be 26 fM. The detailed calculation method was presented in the "Supporting Information". For comparison, several other methods recently reported for CAP determination are listed in Table S4, and the results further confirmed that the developed PEC aptasensor had a wider linear range as well as lower detection limit, indicating its excellent performance with ultrahigh sensitivity. In addition, other performances of the proposed PEC aptasensor including the selectivity, repeatability and stability were also evaluated.

The selectivity assay of the developed PEC aptasensor for CAP

detection was carried out with several possible interfering antibiotics, such as kanamycin (Kana), oxytetracycline (OTC), streptomycin (Strp) and ofloxacin (OFL). The concentration of each interfering antibiotic was 1 nM together with 100 pM of CAP in the experiment, and the tested results are exhibited in Fig. S6A. Compared with the result when only target CAP presented, the photocurrent responses had no significant changes no matter what the interfering antibiotics in single or mixed form were added to the CAP solution. Meanwhile, the relative standard deviations (RSDs) in these measured results were within 3.96%, indicating that the developed PEC aptasensor had a good selectivity for CAP detection.

The repeatability of the constructed PEC aptasensor was assessed by measuring the photocurrent responses of five independently prepared electrodes under the same condition with the CAP concentration at 1 pM, 100 pM and 1 nM, respectively. As shown in Fig. S6B, the RSDs of three different concentrations are 3.2%, 3.6% and 4.3%, respectively. These results suggested that the constructed PEC aptasensor possessed a satisfactory repeatability for CAP monitoring.

The stability of the designed PEC aptasensor was performed by switching the light source on/off for 10 times within 400 s. It could be observed that there was no remarkable photocurrent variation during the period (Fig. S6C). In addition, the PEC response was also measured after the aptasensor was kept at 4 °C in a refrigerator for 2 weeks and the result still maintained about 94% of that the initial photocurrent. These results demonstrated a high stability of the designed PEC aptasensor.

3.8. Real sample analysis

To further assess the feasibility of the aptasensor in real sample applications, the pig urine, river water and milk samples were tested by the aptasensor, and the detail preparation process is described in the "Supporting Information". As displayed in Table S5, the recovery rate of the aptasensor is in the range of 99.06–102.06% with the RSDs of 1.17–3.89%. Meanwhile, HPLC was further employed to verify the reliability of the aptasensor. The HPLC chromatograms of three real samples are shown in Fig. S6, and the detailed analysis method of HPLC is presented in the "Supporting Information". The results of aptasensor are well consistent with those obtained by HPLC, demonstrating that the constructed aptasensor was feasible and has a potential application in real samples for CAP determination.

4. Conclusion

In summary, based on photoactive material of BR-CN and ultrathin PtNi nanozyme, a novel self-powered PEC aptasensor for ultrasensitive CAP detection was constructed successfully. The BR-CN exhibited prominent PEC performance with high photoelectric conversion efficiency, meeting self-powered requirement. And the ultrathin PtNi nanozyme, as a peroxidase mimic, showed superior catalytic performance than HRP and was used to produce catalytic precipitate for signal amplification. Moreover, on the basis of target-induced sensing strategy, the photocurrent value increased with the increasing of CAP concentration. These strategies made this PEC aptasensor achieve ultrasensitive detection for CAP with a detection limit of 26 fM as well as a wide liner range of 0.1 pM–100 nM. Meanwhile, the developed aptasensor exhibited good selectivity, satisfactory reproducibility and high stability, and successfully applied in three real samples. This work provides a novel perspective for the application of nanozyme as an alternative to natural enzyme in the PEC biosensor. The further improvement of nanozyme activities and simplification of the constructions of nanozymes-based PEC biosensors are still in need in the future work.

Declaration of competing interest

The authors declare that they have no known competing financial interests or personal relationships that could have appeared to influence the work reported in this paper.

CRediT authorship contribution statement

Xu Zhu: Conceptualization, Writing - original draft. **Lei Gao:** Methodology. **Lin Tang:** Writing - review & editing. **Bo Peng:** Methodology. **Hongwen Huang:** Writing - review & editing. **Jiajia Wang:** Data curation. **Jiangfang Yu:** Data curation. **Xilian Ouyang:** Formal analysis. **Jisui Tan:** Formal analysis.

Acknowledgements

The study was supported by Projects 51579096 and 51521006 supported by National Natural Science Foundation of China, the Key Research and Development Program of Hunan Province of China (2017SK2241), the National Innovative Talent Promotion Program of China (2017RA2088), the Funds for Innovative Province Construction of Hunan Province of China (2019RS3012) and the National Program for Support of Top-North Young Professionals of China (2012).

Appendix A. Supplementary data

Supplementary data to this article can be found online at https://doi.org/10.1016/j.bios.2019.111756.

References

Chang, G.-R., Chen, H.-S., Lin, F.-Y., 2016. Mar. Pollut. Bull. 113, 579–584.
Chen, Z., Lai, G., Liu, S., Yu, A., 2018. Sens. Actuators, B 273, 1762–1767.
Chen, Z., Ma, G., Chen, Z., Zhang, Y., Zhang, Z., Gao, J., Meng, Q., Yuan, M., Wang, X., Liu, J.-m., 2017. Appl. Surf. Sci. 396, 609–615.
Cheng, W., Pan, J.H., Yang, J.Y., Zheng, Z.Y., Lu, F.S., Chen, Y.W., Gao, W.H., 2018. Microchim. Acta. 185, 10.
Cui, L., Hu, J., Wang, M., Diao, X.-k., Li, C.-c., Zhang, C.-y., 2018. Anal. Chem. 90, 11478–11485.
Deng, Y., Tang, L., Zeng, G., Wang, J., Zhou, Y., Wang, J., Tang, J., Wang, L., Feng, C., 2018. J. Colloid Interface Sci. 509, 219–234.
El-Moghazy, A.Y., Zhao, C., Istamboulie, G., Amaly, N., Si, Y., Noguer, T., Sun, G., 2018. Biosens. Bioelectron. 117, 838–844.
Fan, G.-C., Zhu, H., Du, D., Zhang, J.-R., Zhu, J.-J., Lin, Y., 2016. Anal. Chem. 88, 3392–3399.
Feng, C., Deng, Y., Tang, L., Zeng, G., Wang, J., Yu, J., Liu, Y., Peng, B., Feng, H., Wang, J., 2018. Appl. Catal., B 239, 525–536.
Feng, C., Tang, L., Deng, Y., Zeng, G., Wang, J., Liu, Y., Chen, Z., Yu, J., Wang, J., 2019. Appl. Catal., B 256, 117827.
Fu, X., He, J., Zhang, C., Chen, J., Wen, Y., Mao, W., Zhong, H., Wu, J., Ji, X., Yu, C., 2019. Biosens. Bioelectron. 132, 302–309.
Gao, L., Zhuang, J., Nie, L., Zhang, J., Zhang, Y., Gu, N., Wang, T., Feng, J., Yang, D., Perrett, S., 2007. Nat. Nanotechnol. 2, 577.
Ge, L., Liu, Q., Jiang, D., Ding, L., Wen, Z., Guo, Y., Ding, C., Wang, K., 2019. Biosens. Bioelectron. 135, 145–152.
Gong, L., Dai, H., Zhang, S., Lin, Y., 2016. Anal. Chem. 88, 5775–5782.
Guo, N., Wang, Y., Yan, L., Wang, X., Wang, M., Xu, H., Wang, S., 2017. Water Res. 117, 95–101.
Han, Q., Wang, B., Gao, J., Cheng, Z., Zhao, Y., Zhang, Z., Qu, L., 2016. ACS Nano 10, 2745–2751.
Hu, Z., Yin, Y., Liu, Q., Zheng, X., 2019. Analyst 144, 2716–2724.
Hua, R., Hao, N., Lu, J., Qian, J., Liu, Q., Li, H., Wang, K., 2018. Biosens. Bioelectron. 106, 57–63.
Huang, D., Wang, L., Zhan, Y., Zou, L., Ye, B., 2019. Biosens. Bioelectron. 140, 111358.
Huang, H., Li, K., Chen, Z., Luo, L., Gu, Y., Zhang, D., Ma, C., Si, R., Yang, J., Peng, Z., 2017. J. Am. Chem. Soc. 139, 8152–8159.
Huang, W., Zhang, H., Lai, G., Liu, S., Li, B., Yu, A., 2019. Food Chem. 270, 287–292.
Jiang, Y., Wu, X., Yan, Y., Luo, S., Li, X., Huang, J., Zhang, H., Yang, D., 2019. Small 15, 1805474.
Karim, M.N., Anderson, S.R., Singh, S., Ramanathan, R., Bansal, V., 2018. Biosens. Bioelectron. 110, 8–15.
Kikuchi, H., Sakai, T., Teshima, R., Nemoto, S., Akiyama, H., 2017. Food Chem. 230, 589–593.
Kim, M.S., Cho, S., Joo, S.H., Lee, J., Kwak, S.K., Kim, M.I., Lee, J., 2019. ACS Nano 13, 4312–4321.
Li, K., Li, X., Huang, H., Luo, L., Li, X., Yan, X., Ma, C., Si, R., Yang, J., Zeng, J., 2018. J. Am. Chem. Soc. 140, 16159–16167.
Li, K., Sun, M., Zhang, W.-D., 2018. Carbon 134, 134–144.
Li, W., Fan, G.-C., Gao, F., Cui, Y., Wang, W., Luo, X., 2019. Biosens. Bioelectron. 127, 64–71.
Liu, J., Yu, Y., Qi, R., Cao, C., Liu, X., Zheng, Y., Song, W., 2019. Appl. Catal., B 244, 459–464.

Liu, Y., Liu, Y., Liu, B., 2016. J. Electroanal. Chem. 781, 265–271.
Lu, Y., Yao, H., Li, C., Han, J., Tan, Z., Yan, Y., 2016. Food Chem. 192, 163–170.
Lu, Y., Ye, W., Yang, Q., Yu, J., Wang, Q., Zhou, P., Wang, C., Xue, D., Zhao, S., 2016. Sens. Actuators, B 230, 721–730.
Mu, X.Y., Wang, J.Y., Li, Y.H., Xu, F.J., Long, W., Ouyang, L.F., Liu, H.L., Jing, Y.Q., Wang, J.Y., Dai, H.T., Liu, Q., Sun, Y.M., Liu, C.L., Zhang, X.D., 2019. ACS Nano 13, 1870–1884.
Oh, S., Kim, J., Tran, V.T., Lee, D.K., Ahmed, S.R., Hong, J.C., Lee, J., Park, E.Y., Lee, J., 2018. ACS Appl. Mater. Interfaces 10, 12534–12543.
Peng, B., Tang, L., Zeng, G., Fang, S., Ouyang, X., Long, B., Zhou, Y., Deng, Y., Liu, Y., Wang, J., 2018. Biosens. Bioelectron. 121, 19–26.
Pilehvar, S., Mehta, J., Dardenne, F., Robbens, J., Blust, R., De Wael, K., 2012. Anal. Chem. 84, 6753–6758.
Shang, M., Zhang, J., Qi, H., Gao, Y., Yan, J., Song, W., 2019. Biosens. Bioelectron. 136, 53–59.
Song, P., Xu, H., Wang, J., Zhang, Y., Gao, F., Guo, J., Shiraishi, Y., Du, Y., 2018. Nanoscale 10, 16468–16473.
Song, Y., Qu, K., Zhao, C., Ren, J., Qu, X., 2010. Adv. Mater. 22, 2206–2210.
Sui, N., Li, S., Wang, Y., Zhang, Q., Liu, S., Bai, Q., Xiao, H., Liu, M., Wang, L., William, W.Y., 2019. Microchim. Acta. 186, 186.
Tang, L., Feng, C., Deng, Y., Zeng, G., Wang, J., Liu, Y., Feng, H., Wang, J., 2018. Appl. Catal., B 230, 102–114.
Tang, L., Ouyang, X., Peng, B., Zeng, G., Zhu, Y., Yu, J.F., Feng, C., Fang, S., Zhu, X., Tan, J., 2019. Nanoscale 11, 12198–12209.
Tang, L., Yu, J., Pang, Y., Zeng, G., Deng, Y., Wang, J., Ren, X., Ye, S., Peng, B., Feng, H., 2018. Chem. Eng. J. 336, 160–169.
Wang, G.-L., Shu, J.-X., Dong, Y.-M., Wu, X.-M., Li, Z.-J., 2015. Biosens. Bioelectron. 66, 283–289.
Wang, H., Yin, H., Huang, H., Li, K., Zhou, Y., Waterhouse, G.I., Lin, H., Ai, S., 2018. Biosens. Bioelectron. 108, 89–96.
Wang, H., Zhu, L., Duan, J., Wang, M., Yin, H., Wang, P., Ai, S., 2018. Biosens. Bioelectron. 103, 32–38.
Wang, J., Tang, L., Zeng, G., Deng, Y., Liu, Y., Wang, L., Zhou, Y., Guo, Z., Wang, J., Zhang, C., 2017. Appl. Catal., B 209, 285–294.
Wang, M., Yin, H., Zhou, Y., Sui, C., Wang, Y., Meng, X., Waterhouse, G.I., Ai, S., 2019. Biosens. Bioelectron. 128, 137–143.
Wu, J., Li, N., Zhang, X.-H., Fang, H.-B., Zheng, Y.-Z., Tao, X., 2018. Appl. Catal., B 226, 61–70.
Xu, W., Qin, Z., Hao, Y., He, Q., Chen, S., Zhang, Z., Peng, D., Wen, H., Chen, J., Qiu, J., 2018. Biosens. Bioelectron. 113, 148–156.
Yan, C., Zhang, J., Yao, L., Xue, F., Lu, J., Li, B., Chen, W., 2018. Food Chem. 260, 208–212.
Yang, R., Zou, K., Li, Y., Meng, L., Zhang, X., Chen, J., 2018. Anal. Chem. 90, 9480–9486.
You, F., Zhu, M., Ding, L., Xu, Y., Wang, K., 2019. Biosens. Bioelectron. 130, 230–235.
Yu, J., Tang, L., Pang, Y., Zeng, G., Wang, J., Deng, Y., Liu, Y., Feng, H., Chen, S., Ren, X., 2019. Chem. Eng. J. 364, 146–159.
Yu, Y., Yan, W., Gao, W., Li, P., Wang, X., Wu, S., Song, W., Ding, K., 2017. J. Mater. Chem. 5, 17199–17203.
Yu, Y., Yan, W., Wang, X., Li, P., Gao, W., Zou, H., Wu, S., Ding, K., 2018. Adv. Mater. 30, 1705060.
Zang, Y., Lei, J., Ju, H., 2017. Biosens. Bioelectron. 96, 8–16.
Zhang, W., Yang, Y., Huang, B., Lv, F., Wang, K., Li, N., Luo, M., Chao, Y., Li, Y., Sun, Y., 2019. Adv. Mater. 31, 1805833.
Zhao, W.-W., Ma, Z.-Y., Yu, P.-P., Dong, X.-Y., Xu, J.-J., Chen, H.-Y., 2011. Anal. Chem. 84, 917–923.
Zhou, Z., Zhang, Y., Shen, Y., Liu, S., Zhang, Y., 2018. Chem. Soc. Rev. 47, 2298–2321.